CRYSTAL GROWTH & DESIGN

pubs.acs.org/crystal

Article

Structural Characterization of Tunnel-Structured $MgCO_3·H_2O$ and β-$MgCO_3$: Two-Step Topotactic Dehydration of Nesquehonite Using High Pressure

Ryo Yamane,* Shigeru Suehara, Yoshiki Kiyota, Sadaki Samitsu, and Hiroshi Sakuma

Cite This: *Cryst. Growth Des.* 2026, 26, 3341−3351

Read Online

ACCESS | Metrics & More | Article Recommendations | Supporting Information

ABSTRACT: This study achieved the structural characterization of two novel phases: monohydrated magnesium carbonate (MHMC; $MgCO_3·H_2O$) and a dehydrated phase of MHMC, a previously unknown crystalline polymorph of $MgCO_3$ (β-$MgCO_3$). MHMC was synthesized from nesquehonite (Nq; $MgCO_3·3H_2O$) at 500 MPa and 100 °C, while β-$MgCO_3$ was synthesized by dehydrating MHMC. Due to the fine rod-shaped MHMC and β-$MgCO_3$ crystals, microelectron diffraction was used to characterize the MHMC structure (a = 5.8102(6) Å, b = 5.3759(3) Å, c = 9.259(1) Å, space group: $P2_12_12_1$, calculated density: 2.350 g/cm^3). The $MgCO_3$ rod modules of Nq were polymerized in the MHMC structure, accompanied by dehydration, and MHMC had a tunnel-type $MgCO_3$ framework structure. The structure of β-$MgCO_3$ was theoretically predicted based on the dehydrated MHMC structure and verified by the Rietveld refinement of the powder X-ray diffraction of β-$MgCO_3$ (a = 5.1730(4) Å, b = 5.1597(5) Å, c = 8.8066(5) Å, space group: $P2_12_12_1$, calculated density: 2.383 g/cm^3). The calculated bulk moduli of MHMC and β-$MgCO_3$ were 57.1(1) and 20.0(2) GPa, respectively.

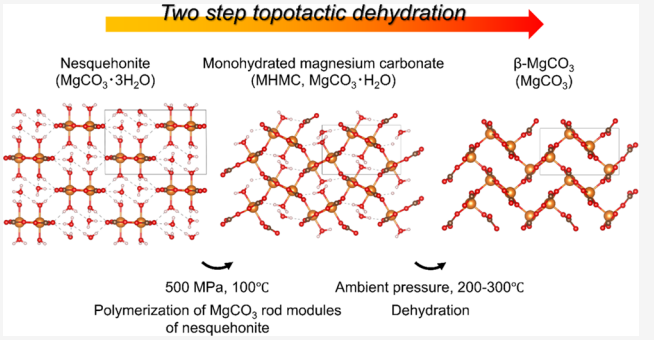

INTRODUCTION

Magnesium carbonates are present in near-surface conditions of the earth during paragenesis and are generated by the carbonation reaction of Mg leached from Mg-rich rocks such as ultramafic rocks or serpentines.[1] This carbonation reaction is fundamental to carbon dioxide (CO_2) fixation. Considering carbon capture, utilization, and storage, developing new functionalities for these reaction products can provide a pathway for their industrial use.

Magnesium carbonates exist as various hydrates,[2] such as the minerals barringtonite, nesquehonite (Nq), and lansfordite, which are represented by $MgCO_3·nH_2O$ (n = 2, 3, and 5), respectively. The partial substitution of CO_3^{2-} by $2OH^-$ further increases their structural variety, resulting in hydrates such as hydromagnesite (Hy; $Mg_5(CO_3)_4(OH)_2·4H_2O$), dypingite ($Mg_5(CO_3)_4(OH)_2·5H_2O$), and artinite ($Mg_2(CO_3)(OH)_2·3H_2O$). Water molecules in hydrated magnesium carbonates (HMCs) break the three-dimensional linkage between Mg^{2+} and CO_3^{2-} and result in anisotropic particle shapes, such as sheets or needles (or rods). Such a form with a high aspect ratio can strengthen polymer composites.[3,4] Because morphology can be maintained after the dehydration of HMCs, the morphological control of magnesium carbonates using various HMC phases has attracted the attention of researchers.

Owing to its rod-shaped morphology,[5] Nq ($MgCO_3·3H_2O$) is used as a precursor to fabricate rod-shaped magnesite ($MgCO_3$) via heating under CO_2 flow.[6] Additionally, a new HMC was recently reported by heating and pressurizing Nq.[7] Under 700 MPa and 115 °C, Santamaria-Perez et al.[7] reported the existence of a new phase, which was identified by in situ X-ray diffraction (XRD) using a diamond-anvil cell (DAC). However, the chemical composition, full characterization, and stability range of the new phase remain unknown. In this study, this new phase is referred to as monohydrated magnesium carbonate (MHMC) after its revealed chemical composition, $MgCO_3·H_2O$.

This study successfully synthesized MHMC using a piston−cylinder-type high-pressure cell with a relatively larger sample volume (typically hundreds of milligrams) compared to that for DACs. Owing to the nanosized crystals of MHMC, its crystal structure was determined using electron diffraction measurements.[8] Based on the unique tunnel-type $MgCO_3$ framework of MHMC, an MHMC dehydration experiment

Received: November 26, 2025
Revised: March 17, 2026
Accepted: March 20, 2026
Published: April 15, 2026

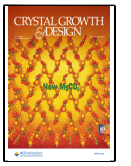

was also performed. Powder XRD (PXRD) revealed the existence of a new $MgCO_3$ phase, and its structural characterization was achieved using a combination of density functional theory (DFT) calculations and Rietveld refinement analyses. Because MHMC and β-$MgCO_3$ can be synthesized under relatively mild pressures and temperatures, they have potential in various applications such as fillers owing to their fine-rod shapes.

EXPERIMENTAL SECTION

Synthesis and Characterization

The synthesis of Nq was performed according to a method described in a previous study.[9] Briefly, a $MgCl_2{\cdot}6H_2O$ solution (24.40 g in 60 mL of distilled water) was added to a Na_2CO_3 solution (12.73 g in 600 mL of distilled water) at 25 °C with stirring at 400 rpm for >9 min. After resting for 12 h under stirring at 400 rpm, Nq was obtained. For MHMC synthesis, Nq was initially compressed to 500 MPa and then heated to 100 °C. The pressure was estimated by dividing the load by the sample area. After 1 h, the compressed samples were cooled to 30 °C, and the pressure was released to ambient pressure. β-$MgCO_3$ was obtained via the heat treatment of MHMC up to 200−300 °C under air or N_2 flow. Notably, "β" indicates the second $MgCO_3$ phase, which was recovered under ambient pressure and temperature conditions; its notation using a Roman numeral is already used for the high-pressure phases of magnesite.[10] The crystal shapes of the samples were observed using field-emission scanning electron microscopy (FE-SEM; S-4800, Hitachi), and PXRD with the Cu-$K\alpha$ doublet (MiniFlex600 or ULTIMA-IV, Rigaku) was conducted to identify the produced phases. To determine the water content of the samples, thermogravimetry/differential thermal analysis (TG-DTA; DTG-60H, Shimadzu) was performed under N_2 flow (100 mL/min) with a heating rate of 20 °C/min. Electron diffraction (ED) was performed using an XtaLAB Synergy-ED equipped with a HyPix-ED detector and the CrysAlis^{Pro} software (JEOL and Rigaku).[8] Raman scattering measurements were obtained using the alpha300 RA system (Oxford Instruments), and porous structures of the samples were characterized via nitrogen gas adsorption at −196 °C using a gas-adsorption analyzer (Belsorp-max, MicrotracBel, Japan). Magnesite was synthesized at 500 MPa and 200 °C (1 h) to compare the PXRD and TG-DTA results with those of MHMC and β-$MgCO_3$. The results of the high-pressure syntheses are shown in Figure 1. Because MHMC is a metastable phase, the synthesis results were dependent on the holding time of the target pressure and temperature. For example, when the MHMC growth time was changed from 1 h to 3 days, the recovered sample transformed into magnesite; therefore, MHMC is thermodynamically metastable to magnesite at 500 MPa and 100 °C. The recovered samples of MHMC and β-$MgCO_3$ showed no significant phase changes under ambient pressure and temperature conditions for at least 9 and 5 months, respectively.

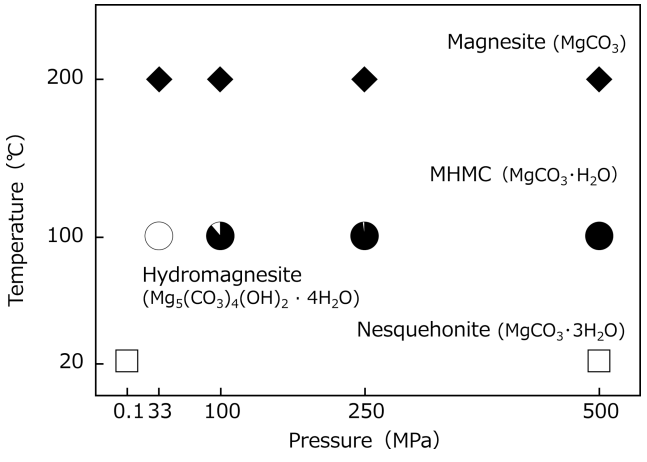

Figure 1. Results of the high-pressure synthesis. Phases: Nq (□), MHMC (●), magnesite (♦), and Hy (○). The pressure is shown on a logarithmic scale. At 100−500 MPa and 100 °C, the coexistence of Hy and MHMC was observed, and their volume fractions are represented by the white and black areas, respectively, of the circles.

Structural Analysis

The lattice parameters and space group (SG) of MHMC were initially examined using PXRD. Le Bail refinement suggested an orthorhombic unit cell with a = 5.8 (Å), b = 5.4 (Å), and c = 9.2 (Å). SGs corresponding to the orthorhombic lattice were considered, and $P2_12_12_1$ was the most plausible based on the reflection conditions $h00$: $h = 2n$, $0k0$: $k = 2n$, and $00l$: $l = 2n$. These results were consistent with the ED measurements, and the lattice parameters of the MHMC were determined from the ED results. Using data collected from ED measurements, structural refinement was conducted and the initial structural model of MHMC was determined via direct methods without hydrogen atoms. Least-squares refinement was performed using the SHELXL software program[11] implemented in WinGX.[12] In the SHELXL program, kinematical refinement is only available. Although the EXTI instruction was applied to account for electron-beam extinction, the dynamical effect in electron diffraction is quite large.[8] To minimize this effect, we carefully selected sufficiently thin samples for data collection. This approach likely contributed to the good agreement obtained between the structural models refined from electron diffraction and X-ray diffraction data, as mentioned after. The SFAC instructions were used to input the atomic scattering factors for the electrons, replacing those for the X-rays.[13] After refining the atomic positions and anisotropic atomic displacement parameters (ADPs) of Mg, C, and O, H atoms were introduced based on the residual peaks. The H atom coordinates were treated with a riding model, and the isotropic ADPs of H were constrained to 1.5× the U_{eq} of adjacent O atoms. Because the diagonal components of the anisotropic ADPs of C were negative values under free restraint conditions, restraint conditions were added between C and one of the O atoms of CO_3^{2-} (O1), assuming they had similar ADPs, using "SIMU" and "RIGU".[11] The structural refinement details, structural parameters, and ADPs of MHMC are listed in Tables 1, 2, and 3, respectively.

The structural refinement of MHMC using PXRD with RIETAN-2000[14] was also performed, yielding results that were consistent with

Table 1. Structure Refinement Details of MHMC

Structural formula	$MgCO_3{\cdot}H_2O$
Temperature	293 K
Crystal system	orthorhombic
Space group	$P2_12_12_1$
Lattice parameters	a = 5.8102(6) Å
	b = 5.3759(3) Å
	c = 9.259(1) Å
Volume (Å^3)	289.20(5)
Z	4
Calculated density (g/cm^3)	2.350
Wavelength (Å)	0.0251
Max. 2θ	1.842°
Index ranges	$-7 \le h \le 7$
	$-6 \le k \le 6$
	$-11 \le l \le 11$
Measured reflections	2048
Data/parameters	588/56
Goodness-of-fit in F^2	1.278
R indices $I > 2\sigma(I)$	0.0901
R indices (all data)	0.0955
$\Delta\rho_{max}/\Delta\rho_{min}$ (eÅ^{-3})	0.154/−0.166

https://doi.org/10.1021/acs.cgd.5c01676
Cryst. Growth Des. 2026, 26, 3341−3351

Table 2. Structural Parameters of MHMC

atom	occupation	x	y	z	U_{eq} (Å^2)
Mg	Mg	0.170(1)	0.151(1)	−0.1203(6)	0.010(1)
O1	O	−0.011(1)	0.871(1)	−0.2635(8)	0.011(1)
O2	O	0.192(2)	0.774(1)	−0.0710(8)	0.010(2)
O3	O	0.067(2)	0.468(1)	−0.2178(9)	0.015(2)
O4	O	−0.146(2)	0.164(2)	−0.0007(8)	0.020(2)
C	C	0.084(2)	0.695(1)	−0.183(1)	0.011(2)
H1	H	−0.11607	0.09466	0.10307	0.03
H2	H	−0.26135	0.08430	−0.05112	0.03

those obtained from the ED measurements (the averaged absolute difference in atomic positions refined with the two measurements was 0.0014 ± 0.0011, Figure S1 and Table S1). However, the positions of H atoms could not be determined using PXRD owing to their low electron density. Therefore, for PXRD refinement, the H positions were fixed to the values obtained from the ED-based refinement. Isotropic ADPs were used, and the ADPs of H atoms were constrained to 1.5× the U of adjacent O atoms. For Rietveld refinement, preferred orientation was assumed regarding the b-axis, which corresponds to the longitudinal direction of MHMC crystals. This assumption was also applied in the Rietveld refinement of β-$MgCO_3$.

A dehydrated MHMC structure, which was optimized through DFT calculations, was employed as the initial structural model of β-$MgCO_3$ used in the Rietveld refinement with RIETAN-2000.[14] For DFT optimization, the refined MHMC structure without water molecules was used. The optimized dehydrated structure of MHMC showed no significant change in symmetry compared with that of $P2_12_12_1$, which is the SG of MHMC. This SG was consistent with that revealed in the PXRD results for β-$MgCO_3$. Moreover, the 2θ regions of 32.2−33.5, 42.2−43.7, and 53.2−55.0 were excluded in Rietveld refinement owing to the coexistence of magnesite. The bond length between C and O in CO_3^{2-} was restrained to 1.29 ± 0.05 Å in the structure, while that between Mg and O1 was 1.99 ± 0.05 Å based on the DFT-optimized structure. Notably, the Mg−O1 length tended to be underestimated to <1.85 Å without restraints, and isotropic ADPs were used. The structural refinement details, structural parameters, and ADPs of β-$MgCO_3$ are presented in Tables 4 and 5.

Computational Details

First-principles DFT calculations were performed to validate the crystal structure and predict the bulk modulus of the newly identified high-pressure phase. All computations employed the Vienna Ab initio Simulation Package (VASP 6.4.2)[15] with the projector-augmented-wave method.[16] The exchange−correlation energy was calculated using the Perdew−Burke−Ernzerhof (PBE) functional within a generalized gradient approximation.[17] To account for long-range van der Waals interactions, Grimme's DFT-D3 dispersion correction with Becke−Johnson damping [PBE+D3(BJ)] was applied.[18] The proposed MHMC (32 atoms) and β-$MgCO_3$ (20 atoms) unit cell structure models were fully optimized using a plane-wave cutoff energy of 520 eV and a Monkhorst−Pack k-point mesh of 6 × 6 × 4[19] for Brillouin zone sampling. The optimized lattice parameters of MHMC were consistent with the experimental diffraction data, with deviations (dev.) of <1% (a = 5.7646 Å (dev.: 0.79%), b = 5.3161 Å (dev.: 1.1%), and c = 9.2313 Å (dev.: 0.30%)). To further characterize the lattice dynamics of the MHMC and β-$MgCO_3$ phases, the phonon density of states of each phase was computed using the finite-displacement method as implemented in the Phonopy package.[20] The absence of imaginary phonon frequencies confirmed the dynamic stability of both the MHMC and β-$MgCO_3$ models. Each 3 × 3 × 2 supercell was employed with a plane-wave cutoff energy of 400 eV and 2 × 2 × 2 k-point mesh. Phonon frequencies on a 30 × 30 × 12 q-point grid were obtained via Fourier interpolation of the dynamic matrix constructed from the force constants derived from the supercell calculations. The isothermal bulk modulus (B_0) was obtained for each phase by fitting the total energy versus volume data, which were calculated at ±1%, ±2%, and ±3% volume changes, to the third-order Birch−Murnaghan equation of state.[21] Furthermore, the unit cell energy of the well-known ambient phase, magnesite (α-$MgCO_3$), was computed using the same DFT setup to compare its relative energetic stability to that of β-$MgCO_3$ (for this phase, γ-centered 6 × 6 × 2 k-point sampling was employed).

Table 4. Structure Refinement Details of β-$MgCO_3$

Structural formula	$MgCO_3$
Temperature	298 K
Crystal system	orthorhombic
Space group	$P2_12_12_1$
Lattice parameters	a = 5.1730(4) Å
	b = 5.1597(5) Å
	c = 8.8066(5) Å
Volume (Å^3)	235.06(3)
Z	4
Calculated density (g/cm^3)	2.383
Wavelength (Å)	1.5418 (Cu-$K\alpha$ doublet)
R_{wp}	7.431
R_p	5.468
S	1.970
R_F	1.274

Table 5. Structural Parameters of β-$MgCO_3$

atom	occupation	x	y	z	U (Å^2)
Mg	Mg	0.1158(9)	0.1425(7)	−0.1228(5)	0.023(1)
O1	O	−0.143(1)	0.882(1)	−0.2076(7)	0.027(2)
O2	O	0.159(1)	0.764(1)	−0.0474(5)	0.010(2)
O3	O	−0.107(2)	0.452(2)	−0.135(1)	0.055(4)
C	C	−0.038(2)	0.690(3)	−0.136(2)	0.015(4)

RESULTS AND DISCUSSION

Morphologies of the MHMC and β-$MgCO_3$ Crystals

Similar to the Nq crystals, the MHMC and β-$MgCO_3$ crystals were characteristically rod-shaped (Figure 2a,b, respectively). No significant change in the crystal shapes between MHMC and β-$MgCO_3$ was observed, and their averaged minor- and major-axis lengths were 160 nm (Figure 2c) and 1.24 μm (Figure 2d), respectively. The averaged aspect ratio (= major length/minor length) was 8.22 (Figure 2e). In recovered

Table 3. ADPs (Å^2) of MHMC

atom	U_{11} (Å^2)	U_{22} (Å^2)	U_{33} (Å^2)	U_{23} (Å^2)	U_{13} (Å^2)	U_{12} (Å^2)
Mg	0.014(4)	0.007(2)	0.008(3)	0.003(2)	0.002(2)	−0.003(2)
O1	0.016(3)	0.003(2)	0.015(3)	0.001(2)	−0.004(3)	−0.001(2)
O2	0.012(4)	0.011(3)	0.008(4)	−0.002(2)	−0.005(3)	−0.002(3)
O3	0.017(5)	0.017(3)	0.011(4)	0.000(3)	−0.006(3)	0.004(3)
O4	0.018(6)	0.027(4)	0.016(4)	0.000(3)	−0.005(3)	−0.005(4)
C1	0.016(4)	0.002(2)	0.015(3)	0.001(2)	−0.004(3)	−0.001(3)

https://doi.org/10.1021/acs.cgd.5c01676
Cryst. Growth Des. 2026, 26, 3341−3351

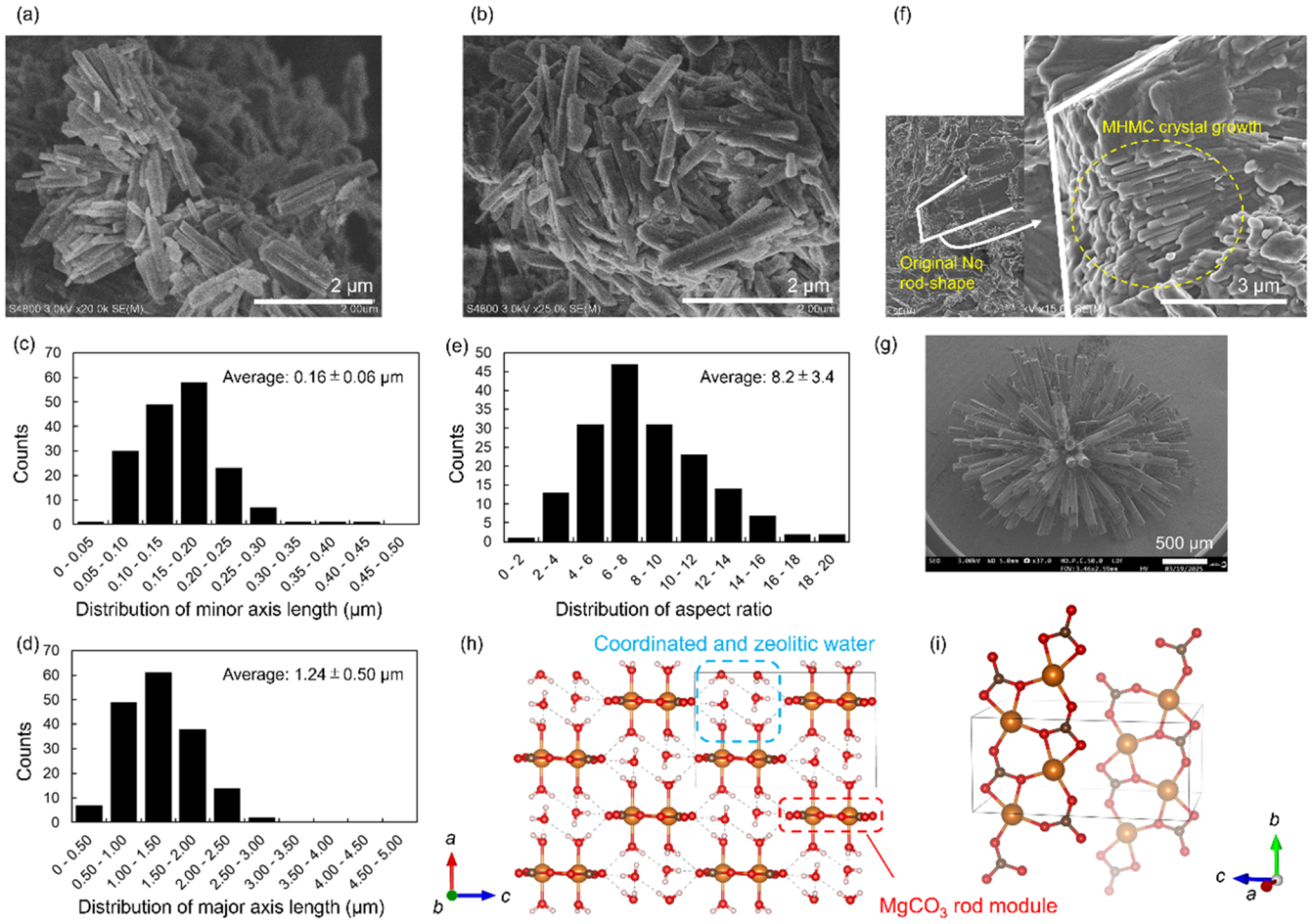

Figure 2. FE-SEM images of (a) MHMC and (b) β-$MgCO_3$. Distributions of the (c) minor axis length, (d) major axis length, and (e) aspect ratio of the rod-like crystals of MHMC and β-$MgCO_3$. Their averaged values and standard deviations are shown in the inset of each figure. (f) FE-SEM image of the Nq sample heated at 80 °C and compressed at 500 MPa. (g) FE-SEM image and (h) crystal structure of Nq. (i) $MgCO_3$ rod modules in the unit cell of Nq (water molecules are not shown). The crystal structure was drawn using VESTA.[22]

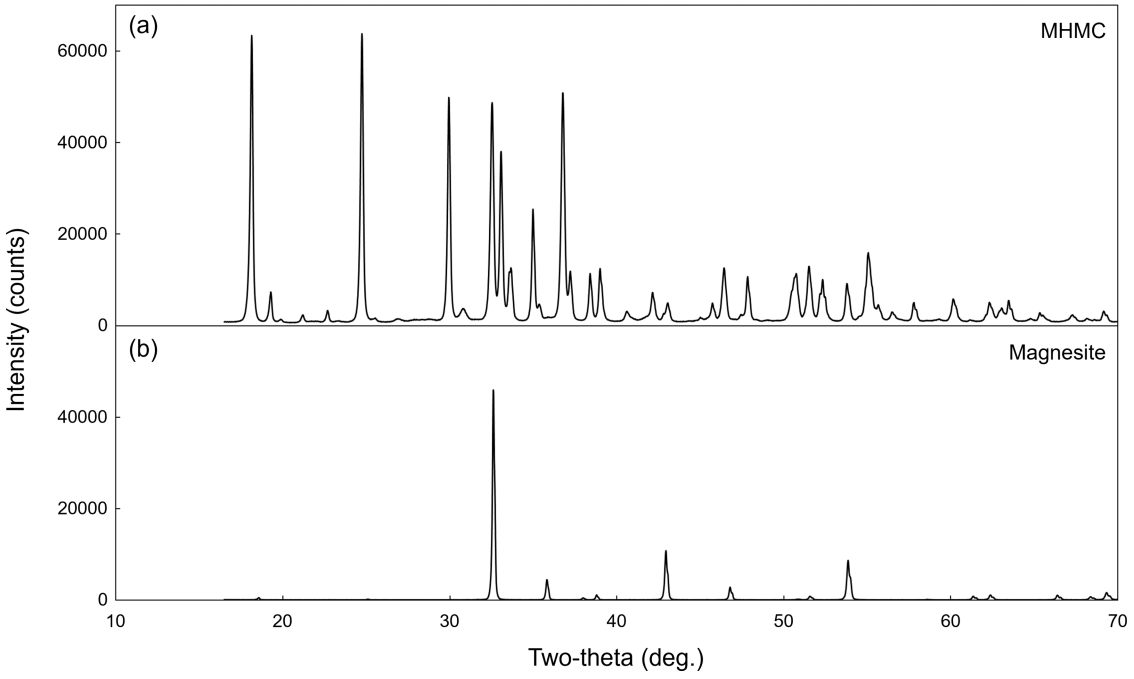

Figure 3. PXRD patterns of (a) MHMC and (b) magnesite.

https://doi.org/10.1021/acs.cgd.5c01676
Cryst. Growth Des. 2026, 26, 3341−3351

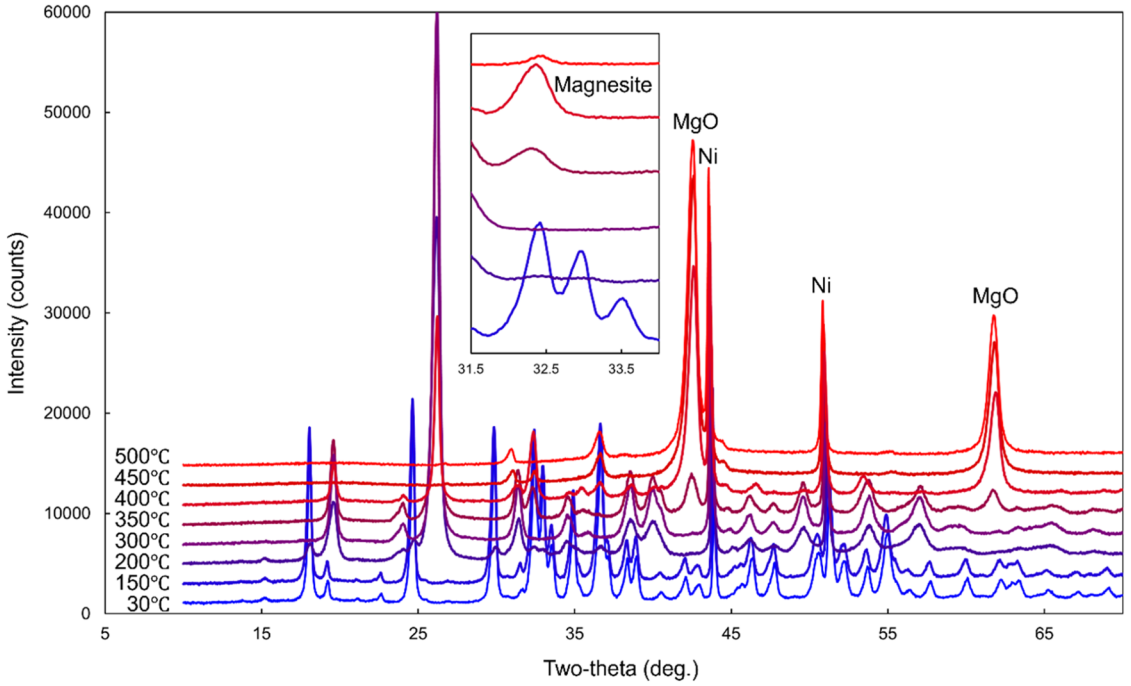

Figure 4. High-temperature PXRD patterns of MHMC. Measurement temperatures are listed on the left side of the corresponding patterns, and the Ni peaks originated from the sample holder.

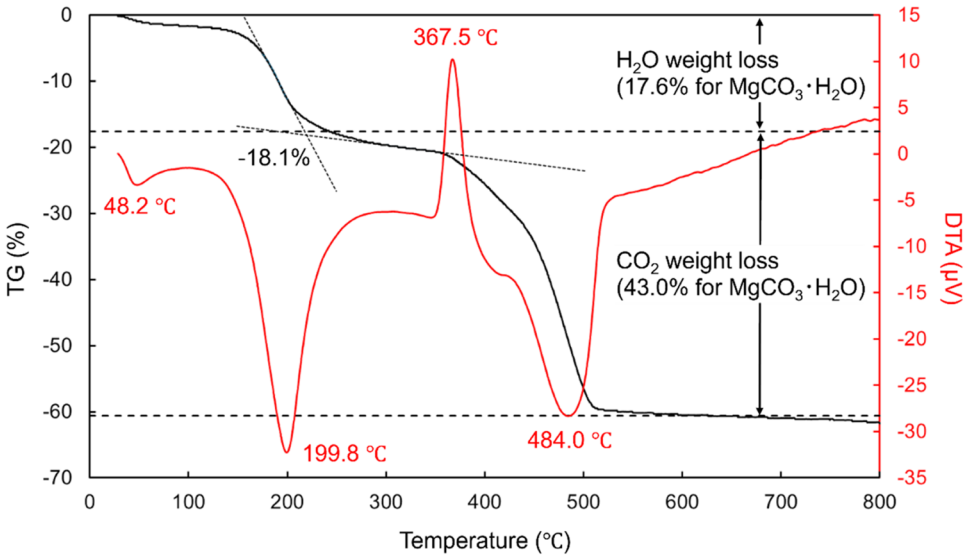

Figure 5. TG (black)/DTA (red) curves of MHMC. In the TG curves, the TG(%) value (−18.1%) of the cross point of the dotted lines was determined as the weight loss of MHMC. In the DTA curves, the top temperatures of each endo/exotherm peak are indicated.

samples that were heated to 80 °C under 500 MPa, crystal growth from Nq to MHMC was observed (Figure 2f). In particular, the Nq crystal split and transformed into MHMC in the same longitudinal direction, as shown in Figure 2f–i. Consequently, the $MgCO_3$ rod modules of Nq were likely maintained during their transformation into MHMC.

Chemical Composition of MHMC

The PXRD pattern of MHMC (Figure 3a) was similar to that previously reported.[7] Santamaria-Perez et al.[7] reported the coexistence of magnesite by comparing the PXRD patterns of magnesite (Figure 3b) with MHMC. Notably, the coexistence of magnesite differed between the synthesis batches. For example, the high-temperature PXRD patterns of the samples presented in Figures 3a,4, and 5 show no sign of the coexistence of magnesite (inset of Figure 4), even though the sample used after the Rietveld refinement of PXRD contained magnesite. Owing to the metastability of MHMC compared to that of magnesite, magnesite can coexist with MHMC during its synthesis.

The TG-DTA, which used the same sample as that used in the high-temperature XRD analysis, revealed a weight loss of the first step at approximately 200 °C, corresponding to the dehydration of one water molecule (Figure 5). The weight loss of the second step (484 °C) corresponded to the decarboxylation of CO_2. This result was consistent with the high-temperature XRD pattern collected at 500 °C, where

https://doi.org/10.1021/acs.cgd.5c01676
Cryst. Growth Des. 2026, 26, 3341−3351

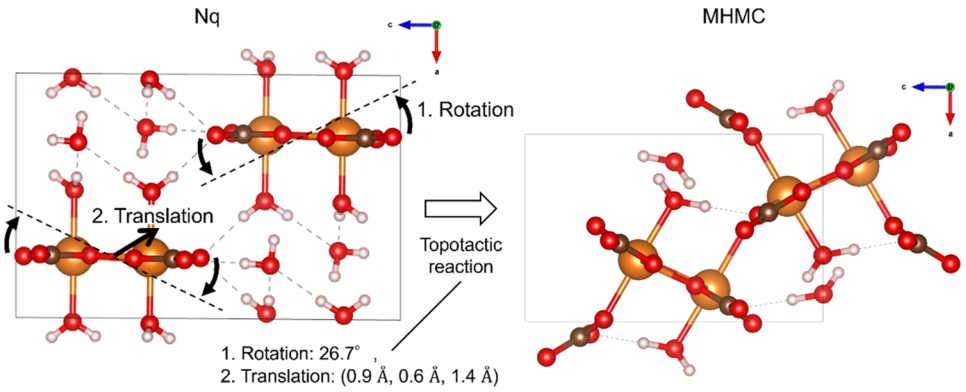

Figure 6. Structural changes in the topotactic reaction of Nq to form MHMC.

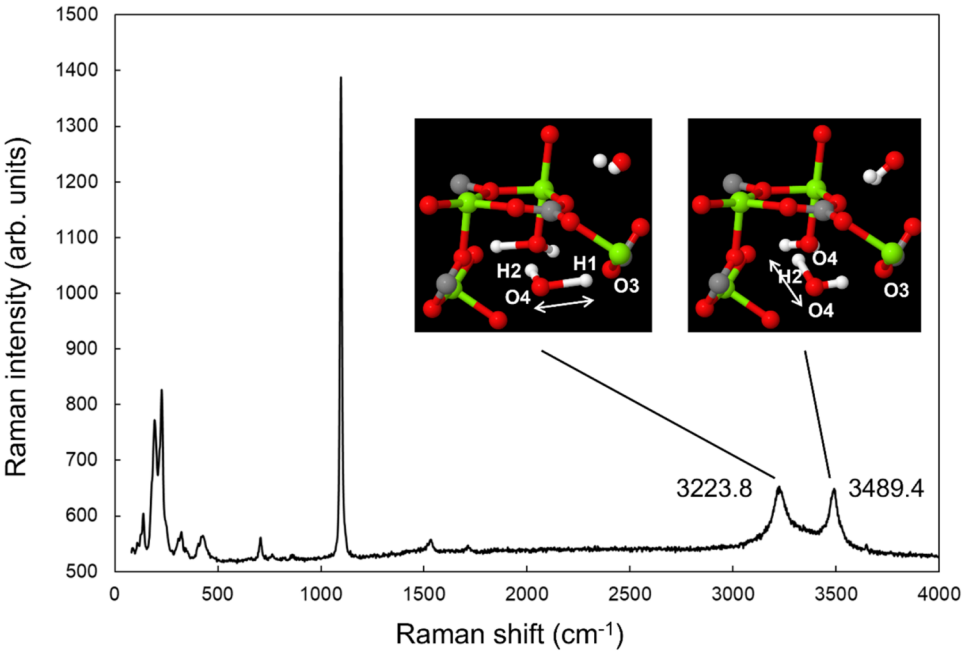

Figure 7. Raman spectrum of MHMC. The inset shows the stretching mode corresponding to peaks at 3223.8 and 3489.4 cm^{-1}. The animation of OH stretching was created using the Jmol software, which is an open-source Java viewer for chemical structures in 3D (http://www.jmol.org/).

MgO (periclase) appeared as the final decomposed material. Therefore, the estimated chemical composition of MHMC was $MgCO_3 \cdot H_2O$, which was consistent with the structural composition determined from the ED measurements (Table 1). Moreover, the MHMC structural model explains the PXRD patterns shown in Figure S1. Notably, a small, unassigned peak was observed at approximately $2\theta = 31°$ in the PXRD patterns collected at 500 °C (Figure 4). Because periclase is a commonly reported stable phase at 500 °C for Nq and Hy, further investigation is required to clarify the origin and assignment of this peak.

Structural Discussion of MHMC: Topotactic Reaction of Nq to Yield MHMC

Considering the revealed structure of MHMC, the structural change from Nq to MHMC can be explained by a topotactic reaction that preserved the *b*-axis of Nq, which is the longitudinal direction of the $MgCO_3$ rod module (Figure 6). In the topotactic reaction, polymerization occurred among $MgCO_3$ rod modules with dehydration, and the polymerization of two $MgCO_3$ rod modules was represented via a combination of two operations: the rotation of 26.7°/−26.7° at the *b*-axis for each module and the translation of (0.9 Å, 0.6 Å, 1.4 Å) from one of the rods to another rod. The Nq lattice was assumed to be orthorhombic (β = ~90.1°), and the position changes of Mg atoms represented the motion of the rod.

The *b*-axis of MHMC was consistent with the longitudinal direction of the rod-shaped MHMC crystal (Figure S2). During the structural change from Nq to MHMC, the lattice parameters of *a* and *c* changed from 7.704 to 5.810 Å and from 12.126 to 9.259(1) Å, respectively. Notably, *b* remained consistent at 5.364 and 5.376 Å for Nq and MHMC, respectively. The *a*−*c* in-plane shrinkage of MHMC generated from the parting (or splitting) of the Nq parent crystal is shown in Figure 2f. Because the area ($a \times c$) of MHMC is 42.3% lower than that of Nq, MHMC grew on an intermediate-like structure of Nq and MHMC crystals rather than directly on the Nq structure.

Structural Discussion of MHMC: Two Types of Hydrogen Bonds in MHMC

In the MHMC structure, water molecules coordinated to Mg atoms and formed hydrogen bonds with neighboring O atoms. In the notations shown in Tables 2 and 3, H1 and H2 formed a

https://doi.org/10.1021/acs.cgd.5c01676
Cryst. Growth Des. 2026, 26, 3341−3351

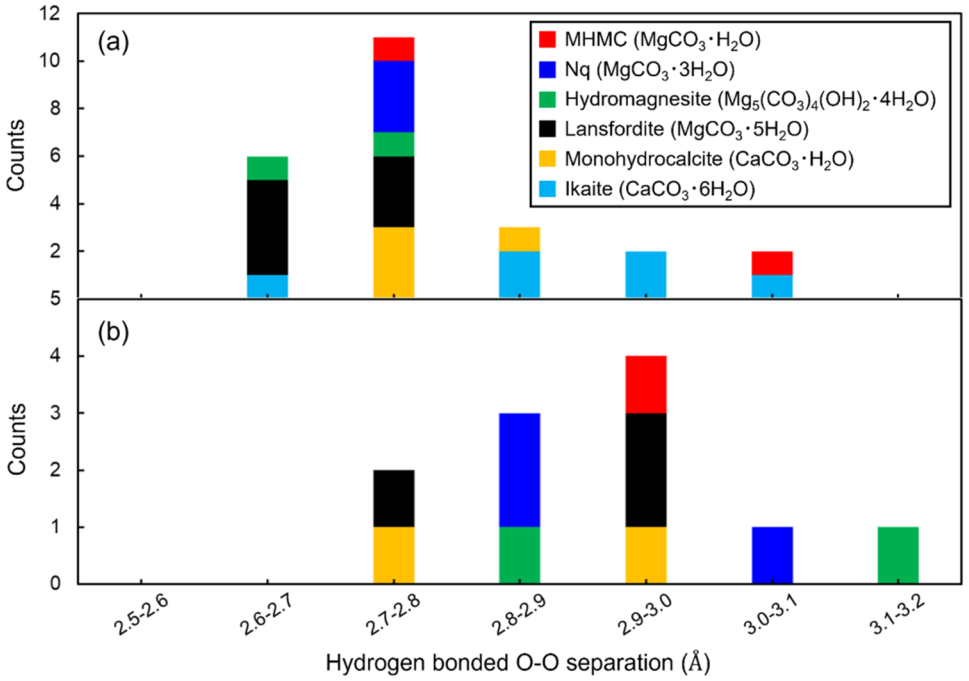

Figure 8. Comparison of hydrogen bonded O−O separations between (a) H_2O and CO_3^{2-} and between (b) H_2O and H_2O in carbonates of Mg and Ca: MHMC (this study), Nq,[24] Hy,[25] lansfordite,[26] monohydrocalcite,[27] and ikaite.[28]

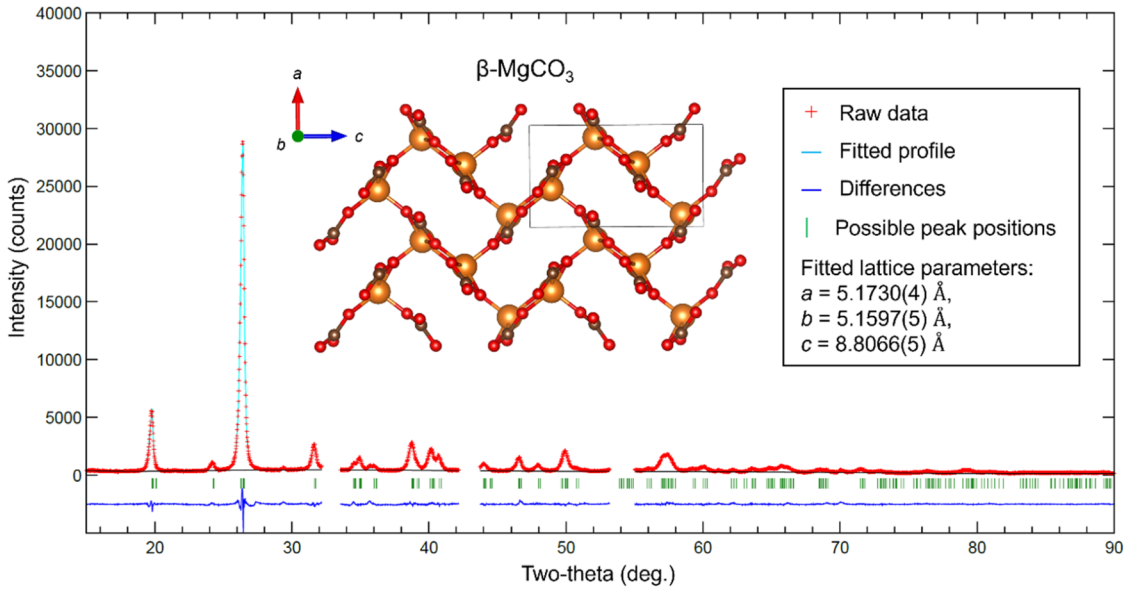

Figure 9. PXRD patterns and Rietveld refinement results of β-$MgCO_3$.

water molecule with O4. Moreover, O3 was the neighboring O atom for H1, and the separation between hydrogen-bonded O atoms was 2.7 Å. For comparison, the typical separation of hydrogen-bonded O atoms is 2.5−3.0 Å.[23] In contrast, H2 had two neighboring O atoms with separations of 2.95 and 3.05 Å for O4 and O1, respectively. Likely owing to comparable and larger separations, the determined H2 position did not form hydrogen bonds between the neighboring O atoms and was in an intermediate position between the O4−O4 and O4−O1 hypothetical bonds. This H2 position might reflect a time- or space-disordered state in terms of H position.

Differences in the nature of the hydrogen bond between H1 and H2 were also observed in the Raman scattering measurements (Figure 7), where two characteristic peaks of the OH stretching mode were observed at approximately 3223.8 and 3489.4 cm^{-1}. The phonon-density calculations were used to reproduce these two peaks (Figure S3). The higher-frequency peak corresponded to O4−H2 stretching, while the lower-frequency peak corresponded to O4−H1 stretching. In the optimized structure, H2 formed a hydrogen bond with O4 but not with O1. In the smaller separation of the hydrogen-bonded O atoms of O4−H1···O3, the O4−H1 covalent bond was weakened, and its stretching peak appeared in the lower-frequency region.

A comparison of the hydrogen-bonded O−O separations between MHMC and other related Mg and Ca carbonates

https://doi.org/10.1021/acs.cgd.5c01676
Cryst. Growth Des. 2026, 26, 3341−3351

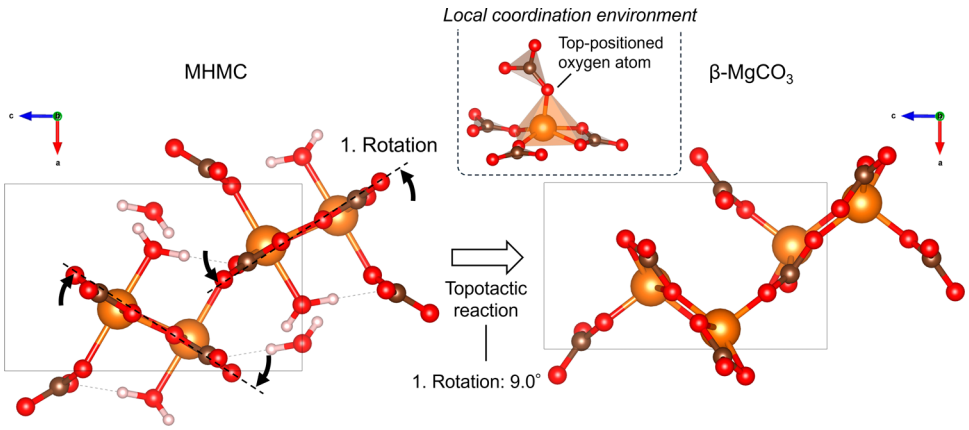

Figure 10. Structural changes in the topotactic reaction of MHMC to yield β-$MgCO_3$.

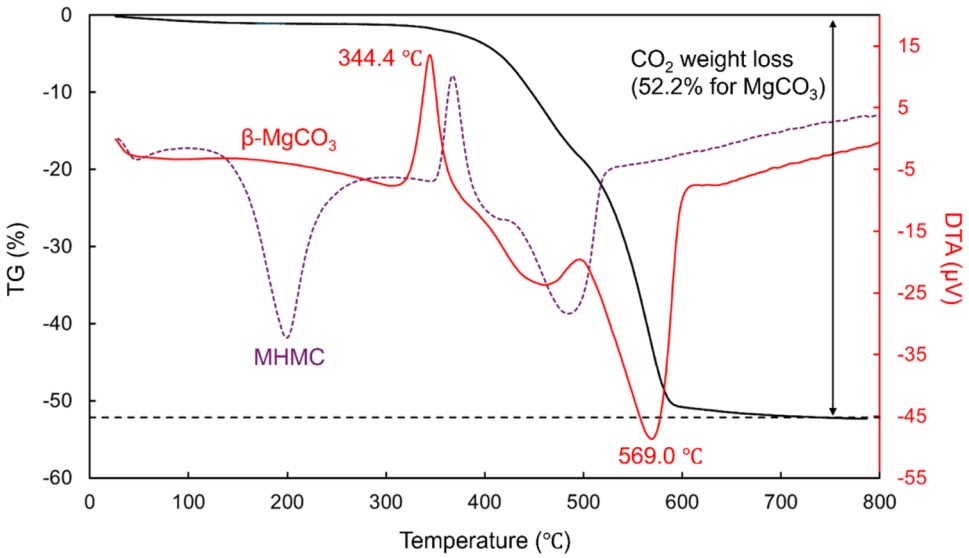

Figure 11. TG (black)/DTA (red) curves of β-$MgCO_3$. The DTA curve of MHMC (Figure 4) is included for comparison. In the DTA curves, the top temperatures of each endo/exotherm peak are indicated.

(Nq, Hy, lansfordite, monohydrocalcite ($CaCO_3 \cdot H_2O$), and ikaite ($CaCO_3 \cdot 6H_2O$)) is shown in Figure 8. In this figure, hydrogen-bonded O−O separations are classified into those between H_2O and CO_3^{2-} (Figure 8a) and those between H_2O and H_2O (Figure 8b). These separations did not depend on the crystal structures or on the cationic size of Ca^{2+} and Mg^{2+}. The average O−O separation for H_2O−CO_3^{2-} hydrogen bonds was 2.78 ± 0.12 Å, which was shorter than that for H_2O−H_2O hydrogen bonds (2.90 ± 0.10 Å). This reflects the stronger negative charge of CO_3^{2-} compared with the lone-pair electrons of the oxygen atom of H_2O. Because each water molecule in these structures forms at least one hydrogen bond with CO_3^{2-}, the H_2O and CO_3^{2-} linkage plays a key role in stabilizing the hydrated carbonate frameworks. The average C−O bond length of CO_3^{2-} was 1.29 ± 0.01 (Å). Therefore, the rigid molecular geometry of CO_3^{2-} was retained in the structures.

Structural Characterization and Discussion of β-$MgCO_3$: Topotactic Reaction of MHMC to Form β-$MgCO_3$

As shown in the high-temperature XRD and TG-DTA results for MHMC (Figures 4 and 5, respectively), β-$MgCO_3$ was obtained via the dehydration of MHMC at 200−300 °C. Considering the crystal structure of MHMC and the similarity of peak positions between MHMC and β-$MgCO_3$, particularly in the 2θ range of 16−35° (Figure 4), the crystal structure of β-$MgCO_3$ was likely the dehydrated tunnel structure of MHMC. Rietveld fitting with the dehydrated tunnel-structured $MgCO_3$ as an initial structural model was used to explain the PXRD patterns of β-$MgCO_3$ (Figure 9). The structural change from MHMC to β-$MgCO_3$ is represented by a rotation of 9.0° around the b-axis for the two modules shown in Figures 6 and 10. Translation was almost negligible (0.0 Å, 0.1 Å, 0.2 Å) for one of the modules, and peak broadening was observed during the transformation. Each full width at half-maximum of the first and second peaks of β-$MgCO_3$ and MHMC were 0.45/0.29 (2θ = 19.6/18.0°) and 0.46/0.30 (2θ = 26.2/24.6°), respectively. This trend was more significant in the higher 2θ region (Figure 4). Thus, dehydration induced structural disorder in β-$MgCO_3$.

Structural Discussion of β-$MgCO_3$: Local Coordination Environment of Mg

A novel coordination environment of Mg appeared in β-$MgCO_3$. Six-coordinated Mg, which is a typical coordination environment of Mg in oxides,[29] turned into five-coordinated Mg through the dehydration of one coordinated water molecule of MHMC. Mg existed in a quadrangular pyramid

https://doi.org/10.1021/acs.cgd.5c01676
Cryst. Growth Des. 2026, 26, 3341−3351

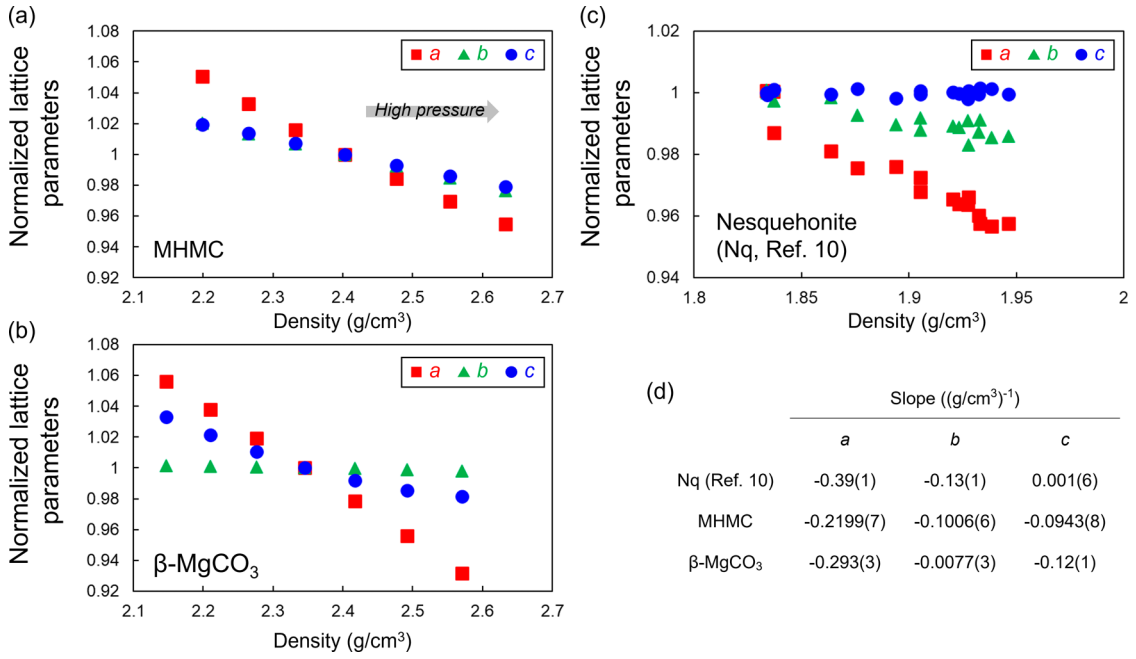

Figure 12. Calculated density dependences of the lattice parameters normalized by those at ambient pressure: (a) MHMC, (b) β-$MgCO_3$, and (c) Nq. The data for Nq were obtained from the Supporting Information in ref 7. (d) Line fitted slopes and their standard deviation of the data shown in (a–c).

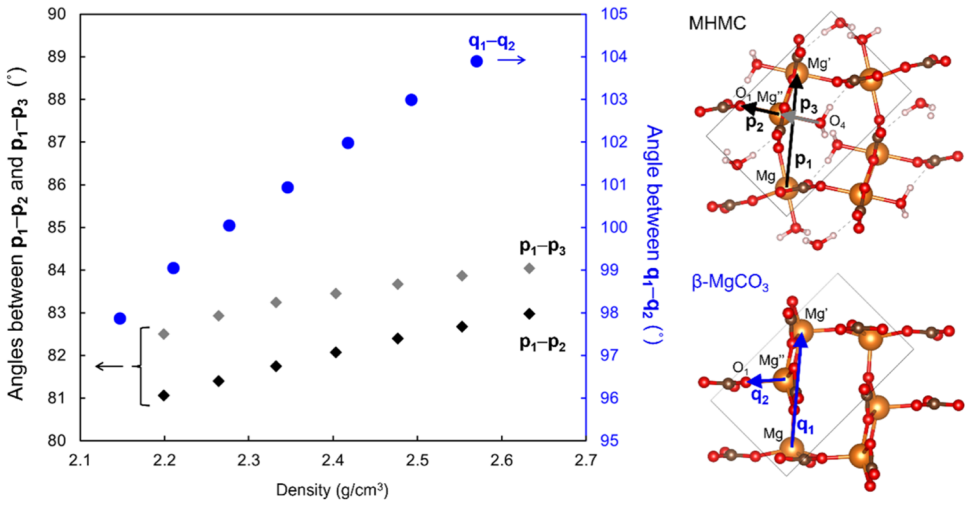

Figure 13. Calculated density dependences of the tunnel structure shrinkages of MHMC and β-$MgCO_3$ characterized by angles between vectors $\mathbf{p_1}$ (from Mg to Mg′) $-\mathbf{p_2}$ (from Mg″ to O_1) and $\mathbf{p_1}-\mathbf{p_3}$ (from O_4 to Mg″) in the MHMC structure and $\mathbf{q_1}$ (from Mg to Mg′) $-\mathbf{q_2}$ (from Mg″ to O_1) in the β-$MgCO_3$ structure. The angles were calculated using the a and c components of the vectors.

in β-$MgCO_3$, and the bond length between Mg and the top-positioned O atom (O1) was 1.950(8) Å (Figure 10). The corresponding Mg–O1 length was 2.147(1) Å in the MHMC structure, while the Mg–O4 (water) coordination length was 2.146(1) Å. The disappearance of the Coulomb interaction between Mg and O4 caused the Mg atom to shift 0.2 Å toward O1. With this displacement of Mg, the quadrangle shrank in size from MHMC to β-$MgCO_3$; consequently, the average Mg–O length of the quadrangle changed from 2.10 to 2.02 Å, respectively.

Thermal Behavior of β-$MgCO_3$

The thermal stability of β-$MgCO_3$ was verified using TG-DTA measurements (Figure 11). β-$MgCO_3$ was stable up to 300 °C and exhibited a characteristic exotherm peak at approximately 350 °C. Above this temperature, β-$MgCO_3$ turned into magnesite and periclase, as confirmed from the high-temperature XRD results of MHMC (Figure 4). Because magnesite showed no exotherm peak during heating,[30] the exotherm peak was assigned to the phase transition from β-$MgCO_3$ to magnesite (i.e., α-$MgCO_3$). The calculated difference in the ground state energies of β-$MgCO_3$ and magnesite was 29.9 kJ/mol, and magnesite was the more stable phase. Because the calculated β-$MgCO_3$ density was 2.38 g/cm^3 (magnesite: 3.0 g/cm^3),[31] the topotactic dehydration of MHMC to β-$MgCO_3$ changed to the nontopotactic dehydration of MHMC to α-$MgCO_3$ under a higher-pressure region (<100 MPa, Figure 1).

https://doi.org/10.1021/acs.cgd.5c01676
Cryst. Growth Des. 2026, 26, 3341–3351

Porous Nature of β-$MgCO_3$ and Bulk Modulus Comparisons among Nq, MHMC, and β-$MgCO_3$

The structural change from MHMC to β-$MgCO_3$ tended to reduce the pore size of the tunnel structure (pore size of β-$MgCO_3$ was ∼3 × 7 Å in atomic separations). The specific surface area of β-$MgCO_3$ was 13 m^2/g, and β-$MgCO_3$ showed no signs of microporous behavior (Figure S4). The effective pore size of the tunnel structure was not large enough for the N_2 molecules to exhibit microporous behavior.

The estimated bulk moduli (B_0) of MHMC and β-$MgCO_3$ were 57.1(1) (equilibrium volume (V_0): 284.5 $Å^3$, pressure derivative (B_0'): 5.5) and 20.0(2) GPa (V_0: 241.2 $Å^3$, B_0': 6.4), respectively. Moreover, the dehydration of MHMC caused softening in the $a-c$ plane vertical to the tunnel longitudinal direction (Figure 12). The bulk modulus of MHMC was higher than that of Nq (exp.: 24(2) GPa, theor.: 38.2(5) GPa).[7] Polymerization created a three-dimensional linkage between Mg^{2+} and CO_3^{2-} and hardened MHMC more than Nq. Additionally, the existence of water molecules in the tunnel framework resulted in relatively isotropic compressibility among the three axes compared to those of Nq and β-$MgCO_3$ (Figure 12). The greater hardness of MHMC compared to that of β-$MgCO_3$ is due to steric effects associated with Mg−O octahedra in the MHMC structure. Under compression, atomic rearrangements retained the coordination polyhedra. Our structural analysis (Figure 13) revealed that the pentahedral structure in β-$MgCO_3$ could move (rotate) relatively easily within the $a-c$ plane, folding inward toward the cavity. Conversely, the octahedral structure in MHMC was much more constrained. This observation was partially attributed to the loss of restrictions on the motion of water molecules, which coordinate to Mg and form H bonds in the cavity.

Possible Existence of Other Tunnel Structures in HMCs

Hy ($Mg_5(CO_3)_4(OH)_2{\cdot}4H_2O$) also contains a tunnel (or channel) framework that includes water molecules and the hydroxy anion.[25] In a previous study, Hy was transformed into a structurally random phase via dehydration, and the dehydrated Hy phase exhibited a Bragg pattern similar to that of Hy.[32] The dehydrated product maintained atomic correlation in the middle-range order (<∼5 Å), as evidenced by its pair-distribution function analysis. Thus, the Hy tunnel structure was likely retained, and a novel quadrangular pyramid coordination of Mg possibly existed in the dehydrated Hy structure. This study highlights the combination of theoretical structural prediction and experimental verification as a powerful tool to reveal such dehydration-induced disordered structures.

CONCLUSION

This study reports a new polymorph of magnesium carbonate inspired by the newly revealed structure of MHMC ($MgCO_3{\cdot}H_2O$), which has the densest structure among all known HMCs. MHMC was synthesized from Nq but could not be obtained from Hy, indicating that the $MgCO_3$ rod modules of Nq were intrinsically important for MHMC synthesis. The high aspect ratio of the crystals and the calculated bulk modulus of MHMC are promising characteristics for its potential application in fillers. Moreover, the novel coordination environment of Mg in the β-$MgCO_3$ structure provides a structural example of metastable dehydrated products with unique local structures.

ASSOCIATED CONTENT

Supporting Information

The Supporting Information is available free of charge at https://pubs.acs.org/doi/10.1021/acs.cgd.5c01676.

Additional experimental and computational results, including Rietveld refinement results, sample photographs of the electron diffraction measurements, phonon-density calculations of MHMC, and specific surface area data for β-$MgCO_3$ (PDF)
DFT optimized β-$MgCO_3$ (CIF)
DFT optimized MHMC (CIF)

Accession Codes

Deposition Numbers 2505847 and 2506022 contain the supplementary crystallographic data for this paper. These data can be obtained free of charge via the joint Cambridge Crystallographic Data Centre (CCDC) and Fachinformationszentrum Karlsruhe Access Structures service.

AUTHOR INFORMATION

Corresponding Author

Ryo Yamane − *Environmental Circulation Composite Materials Group, National Institute for Materials Science (NIMS), Tsukuba, Ibaraki 305-0044, Japan;* orcid.org/0000-0001-9953-5280; Email: YAMANE.Ryo@nims.go.jp

Authors

Shigeru Suehara − *Environmental Circulation Composite Materials Group, National Institute for Materials Science (NIMS), Tsukuba, Ibaraki 305-0044, Japan*

Yoshiki Kiyota − *Rigaku Corporation, Akishima, Tokyo 196-8666, Japan*

Sadaki Samitsu − *Research Center for Macromolecules and Biomaterials, National Institute for Materials Science, Tsukuba, Ibaraki 305-0047, Japan;* orcid.org/0000-0002-4139-1656

Hiroshi Sakuma − *Environmental Circulation Composite Materials Group, National Institute for Materials Science (NIMS), Tsukuba, Ibaraki 305-0044, Japan;* orcid.org/0000-0002-6522-0704

Complete contact information is available at: https://pubs.acs.org/10.1021/acs.cgd.5c01676

Author Contributions

R.Y. conceived and designed the experiments and wrote the manuscript with contributions from H.S. Y.K. conducted the ED experiments. R.Y. and Y.K. conducted the structural analysis of MHMC. R.Y. and S(a).S(a). conducted the BET specific surface area experiments. S(h).S(u). conducted the DFT calculations. All authors discussed the data interpretation.

Notes

The authors declare no competing financial interest.

ACKNOWLEDGMENTS

We are grateful to Rigaku. Corp. for allowing us to use Synergy-ED. This study was supported by JSPS KAKENHI (grant number: JP22K14750).

ABBREVIATIONS

ADP, atomic displacement parameter; DAC, diamond-anvil cell; dev., deviation; DFT, density functional theory; ED,

electron diffraction; FE-SEM, field-emission scanning electron microscopy; HMC, hydrated magnesium carbonate; Hy, hydromagnesite; MHMC, monohydrated magnesium carbonate; Nq, nesquehonite; PBE, Perdew−Burke−Ernzerhof; PXRD, powder X-ray diffraction; SG, space group; TG-DTA, thermogravimetry/differential thermal analysis; XRD, X-ray diffraction

REFERENCES

(1) Ugapeva, S. S.; Oleinikov, O. B.; Zayakina, N. V. Rare hydrated magnesium carbonate minerals nesquehonite and dypingite of the Obnazhennaya kimberlite pipe, in the Yakutian kimberlite province. *Minerals* **2023**, *13* (11), No. 1363.

(2) German, A.; Winnefeld, F.; Lura, P.; Rentsch, D.; Lothenbach, B. Hydrous carbonate-containing brucite (HCB) in MgO/hydromagnesite blends. *Cem. Concr. Res.* **2023**, *173*, No. 107304.

(3) Halpin, J. C.; Tsai, S. *Effects of Environmental Factors on Composite Materials*; Air Force Materials Laboratory Technical Report, 1969; 423.

(4) Sakuma, H.; Suehara, S.; Nakao, H.; Kim, J. D.; Tamura, K. Synthesis of needle−like aragonite using carbonation method: a review. *J. Mineral. Petrol. Sci.* **2025**, *120* (1), No. 240819, DOI: 10.2465/JMPS.240819.

(5) Genth, F. A.; Penfield, S. L. On Lansfordite, nesquehonite, a new mineral, and pseudomorphs of nesquehonite after lansfordite. *Am. J. Sci.* **1890**, *3* (230), 121−137.

(6) Nakamura, M. Acicular Anhydrous Magnesium Carbonate and Method for Producing Sam and Resin Composition. WO Patent WO2019/044066A1, 2019.

(7) Santamaría-Pérez, D.; Chuliá-Jordán, R.; Gonzalez-Platas, J.; Otero-De-La-Roza, A.; Ruiz-Fuertes, J.; Pellicer-Porres, J.; Oliva, R.; Popescu, C. Polymorphism and phase stability of hydrated magnesium carbonate nesquehonite $MgCO_3{\cdot}3H_2O$: negative axial compressibility and thermal expansion in a cementitious material. *Cryst. Growth Des.* **2024**, *24* (3), 1159−1169.

(8) Ito, S.; White, F. J.; Okunishi, E.; Aoyama, Y.; Yamano, A.; Sato, H.; Ferrara, J. D.; Jasnowski, M.; Meyer, M. Structure determination of small molecule compounds by an electron diffractometer for 3D ED/MicroED. *CrystEngComm* **2021**, *23* (48), 8622−8630.

(9) Jauffret, G.; Morrison, J.; Glasser, F. P. On the thermal decomposition of nesquehonite. *J. Therm. Anal. Calorim.* **2015**, *122* (2), 601−609.

(10) Isshiki, M.; Irifune, T.; Hirose, K.; Ono, S.; Ohishi, Y.; Watanuki, T.; Nishibori, E.; Takata, M.; Sakata, M. Stability of magnesite and its high-pressure form in the lowermost mantle. *Nature* **2004**, *427* (6969), 60−63.

(11) Sheldrick, G. M. Crystal structure refinement with SHELXL. *Acta Crystallogr. Sect. C Struct. Chem.* **2015**, *71* (1), 3−8.

(12) Farrugia, L. J. WinGX and ORTEP for windows: an update. *J. Appl. Crystallogr.* **2012**, *45* (4), 849−854.

(13) Peng, L. M. Electron atomic scattering factors and scattering potentials of crystals. *Micron* **1999**, *30* (6), 625−648.

(14) Izumi, F.; Momma, K. Three-dimensional visualization in powder diffraction. *Solid State Phenom.* **2007**, *130*, 15−20.

(15) Kresse, G.; Furthmüller, J. Efficiency of ab-initio total energy calculations for metals and semiconductors using a plane-wave basis set. *Comput. Mater. Sci.* **1996**, *6* (1), 15−50.

(16) Blöchl, P. E. Projector augmented-wave method. *Phys. Rev. B Condens. Matter* **1994**, *50* (24), 17953−17979.

(17) Perdew, J. P.; Burke, K.; Ernzerhof, M. Generalized gradient approximation made simple. *Phys. Rev. Lett.* **1996**, *77* (18), 3865−3868.

(18) Grimme, S.; Ehrlich, S.; Goerick, L. Software news and updates Gabedit—A graphical user interface for computational chemistry software. *J. Comput. Chem.* **2012**, *32*, 174−182.

(19) Pack, J. D.; Monkhorst, H. J. Special points for Brillouin-zone integrations'—a reply. *Phys. Rev. B* **1977**, *16* (4), 1748−1749.

(20) Togo, A.; Chaput, L.; Tadano, T.; Tanaka, I. Implementation strategies in phonopy and phono3py. *J. Phys.: Condens. Matter* **2023**, *35* (35), No. 353001.

(21) Birch, F. Finite elastic strain of cubic crystals. *Phys. Rev.* **1947**, *71* (11), 809−824.

(22) Momma, K.; Izumi, F. V. VESTA 3 for three-dimensional visualization of crystal, volumetric and morphology data. *J. Appl. Crystallogr.* **2011**, *44* (6), 1272−1276.

(23) Pimentel, G. C.; McClellan, A. L. Hydrogen bonding. *Annu. Rev. Phys. Chem.* **1971**, *22* (1), 347−385.

(24) Giester, G.; Lengauer, C. L.; Rieck, B. The crystal structure of nesquehonite, $MgCO_3 \cdot 3H_2O$, from Lavrion, Greece. *Miner. Petrol.* **2000**, *70*, 153−163.

(25) Akao, M.; Iwai, S. The hydrogen bonding of hydromagnesite. *Sci. China Chem.* **1990**, *33* (11), 1350−1356.

(26) Liu, B. N.; Zhou, X. T.; Cui, X. S.; Tang, J. G. Synthesis of lansfordite $MgCO_3{\cdot}5H_2O$ and its crystal structure investigation. *Acta Crystallogr. B* **1988**, *44* (4), 362−367.

(27) Swainson, I. P. The structure of monohydrocalcite and the phase composition of the beachrock deposits of Lake Butler and Lake Fellmongery, South Australia. *Am. Mineral.* **2008**, *93* (7), 1014−1018.

(28) Hesse, K. F.; Kuppers, H.; Suess, E. Refinement of the structure of ikaite, $CaCO_3{\cdot}6(H_2O)$. *Z. Kristallogr. Cryst. Mater.* **1983**, *163* (3−4), 227−231.

(29) Marcus, Y. Ionic radii in aqueous solutions. *Chem. Rev.* **1988**, *88* (8), 1475−1498.

(30) Hycnar, E.; Sęk, M.; Ratajczak, T. Magnesite as a sorbent in fluid combustion conditions—role of magnesium in SO_2 sorption process. *Minerals* **2023**, *13* (3), No. 442.

(31) Göttlicher, S.; Vegas, A. Electron-density distribution in magnesite ($MgCO_3$). *Acta Crystallogr. B* **1988**, *44* (4), 362−367.

(32) Yamamoto, G.-i.; Kyono, A.; Sano, Y.; Matsushita, Y.; Yoneda, Y. In situ and ex situ studies on thermal decomposition process of hydromagnesite $Mg_5(CO_3)_4(OH)_2{\cdot}4H_2O$. *J. Therm. Anal. Calorim.* **2021**, *144* (3), 599−609.

https://doi.org/10.1021/acs.cgd.5c01676
Cryst. Growth Des. 2026, 26, 3341−3351